TU Delft

Delft University of Technology

Document Version
Final published version

Licence
CC BY

Citation (APA)
Hoffstaedt, J. P., Jarquin Laguna, A., Ansorena Ruiz, R., Schürenkamp, D., Goseberg, N., Truijen, D. P. K., De Kooning, J. D. M., Stockman, K., Fahlbeck, J., & Nilsson, H. (2025). Analysis of a contra-rotating pump–turbine for low-head applications: An experimental study and numerical comparison. *Energy Conversion and Management*, *341*, Article 119950. https://doi.org/10.1016/j.enconman.2025.119950

Important note
To cite this publication, please use the final published version (if applicable).
Please check the document version above.

Copyright
In case the licence states “Dutch Copyright Act (Article 25fa)”, this publication was made available Green Open Access via the TU Delft Institutional Repository pursuant to Dutch Copyright Act (Article 25fa, the Taverne amendment). This provision does not affect copyright ownership.
Unless copyright is transferred by contract or statute, it remains with the copyright holder.

Sharing and reuse
Other than for strictly personal use, it is not permitted to download, forward or distribute the text or part of it, without the consent of the author(s) and/or copyright holder(s), unless the work is under an open content license such as Creative Commons.

Takedown policy
Please contact us and provide details if you believe this document breaches copyrights.
We will remove access to the work immediately and investigate your claim.

*This work is downloaded from Delft University of Technology.*

Energy Conversion and Management 341 (2025) 119950

Contents lists available at ScienceDirect

Energy Conversion and Management

journal homepage: www.elsevier.com/locate/enconman

Research paper

# Analysis of a contra-rotating pump–turbine for low-head applications: An experimental study and numerical comparison

J.P. Hoffstaedt [a,*], A. Jarquin Laguna [a], R. Ansorena Ruiz [b], D. Schürenkamp [b], N. Goseberg [b,c], D.P.K. Truijen [d,e], J.D.M. De Kooning [d,e], K. Stockman [d,e], J. Fahlbeck [f], H. Nilsson [f]

[a] Faculty of Mechanical Engineering, Department of Maritime and Transport Technology, Delft University of Technology, Mekelweg 2, 2628 CD Delft, The Netherlands
[b] Leichtweiß-Institute for Hydraulic Engineering and Water Resources, Technische Universität Braunschweig, Braunschweig, Germany
[c] Coastal Research Center, Joint Research Facility of Leibniz University Hannover and Technische Universität Braunschweig, Hannover, Germany
[d] Department of Electromechanical, Systems & Metal Engineering, Ghent University, 8500 Kortrijk, Belgium
[e] FlandersMake@UGent–Corelab MIRO, Flanders Make, Belgium
[f] Department of Mechanics and Maritime Sciences, Division of Fluid Dynamics, Chalmers University of Technology, 412 96 Gothenburg, Sweden

ARTICLE INFO

*Keywords:*
Reversible pump–turbine
Experimental testing
Physical modelling
Fluid transients
Low-head pumped hydro storage
Energy storage

ABSTRACT

Low-head pumped hydro storage technology has been identified as a promising contributor to grid-scale energy storage and the provision of ancillary services. Low-head systems have differing characteristics compared to conventional high-head systems, including larger relative head ranges and increased inertias of both, the water column and the pump–turbines. These differences require new designs as well as a detailed evaluation of their steady-state performance and transient behaviour. For this purpose, an experimental 50kW setup incorporating a 1:22 scale version of a novel reversible pump–turbine, with two contra-rotating runners and independent drivetrains, is designed and constructed. Steady-state performance tests are conducted in turbine and pump modes for several speed ratios between runners. Using head and torque coefficients, the results are compared to a numerical pump–turbine model based on a range of computational fluid dynamics simulations. Additionally, the transient response for a change of operating points is tested and used to benchmark a 1-D numerical model covering dynamic effects including coupling between the conduit and drivetrains. The developed numerical model is then used to simulate the transient behaviour during a shutdown sequence in turbine mode. During the steady-state tests a maximum efficiency of 89% was measured in turbine mode and 92% in pump mode. The test results show that the steady-state RPT characterisation accurately predicts the RPT performance, particularly in turbine mode, with correlation coefficient values between 0.9–0.97. The comparison of the pump mode results shows a minor offset and difference in the correlation between experimental and numerical results. Similarly, the comparison of the transient test case shows a good agreement between the experimental and the simulated dynamic response of the flow rate and rotational speeds. The results have shown the capability of the numerical modelling approach to provide accurate results for steady-state and dynamic performance evaluations. Finally, the simulation of the shutdown sequence indicates that there is no risk of dangerous pressure transients during the desired deceleration of the runners and concurrent closure of the valve.

## 1. Introduction

Setting aside political and financial obstacles, two primary technological challenges must be overcome to decarbonise our electrical power generation and consumption. These are the intermittency and variability of renewable energy sources, as well as the reduction of grid inertia caused by increasing shares of inverter coupled renewable energy sources [1]. To ensure a stable and reliable power grid, large-scale energy storage solutions are required that are able to rapidly absorb and redistribute electrical energy from the grid [2]. Such systems should therefore not only be able to perform load shifting on larger timescales but also contribute to grid stability through fast changes of their power set points and between storage and generation modes.

* Corresponding author.
*E-mail address:* J.P.Hoffstaedt@tudelft.nl (J.P. Hoffstaedt).

https://doi.org/10.1016/j.enconman.2025.119950
Received 4 December 2024; Received in revised form 18 April 2025; Accepted 14 May 2025
Available online 5 June 2025
0196-8904/© 2025 The Authors. Published by Elsevier Ltd. This is an open access article under the CC BY license (http://creativecommons.org/licenses/by/4.0/).

Many energy storage technologies are being investigated for their suitability to be deployed on a large scale [3,4]. Among these, low-head pumped hydro storage has been identified as a promising solution [1], suitable to low-land regional contexts where large elevation gradients are missing. By shifting the operating range from conventional high-head applications, typically 100 m to 800 m [5], to low-heads, i.e. 2 m to 20 m, the goal is to realise the benefits of pumped hydro storage technology in regions without significant topographical features, such as large achievable capacities and long lifetimes. Longer lifetimes compared to other storage technologies in combination with a low carbon density as well as other economic and environmental factors have seen pumped hydro storage ranked as the most sustainable energy storage method [6]. Additional advantages are flexible operation including fast switch-on and switch-off times and the capability for long-term storage since almost no storage losses occur.

However, low-head storage systems significantly differ in their operational characteristics. Compared to the proven and mature technology of traditional high-head systems, low-head storage systems experience much larger relative changes in gross head [7]. Designing pump–turbines capable of delivering high efficiencies over this wide operating range is a key challenge. Low-head systems often also require a higher number of pump and/or turbine units, thus, putting pressure on specific design requirements or on the efficiency of the hydraulic machinery. Hence, combined pump–turbine machinery may become a viable solution to obtain more sustainable technology. Low-head systems are also characterised by larger flow rates for a given desired power capacity. This in turn can lead to undesirable transient effects, also known as water hammer effects [8], which are more likely to occur due to the larger inertia of the water column in the conduit. The larger flow rates also lead to larger machinery and with that increased rotational inertia from their respective drivetrains. Lastly, low-head systems are inherently more prone to cavitation [9,10], since a lower static pressure increases the risk of the effect occurring [11]. This is particularly relevant during pump operation at the suction side of the pump–turbine. Utilising a low-head pumped storage system for load shifting and the provision of frequency regulation services requires significant technological innovation to tackle these challenges. An overview of the technical aspects which include the design of the machinery and civil structures, the control and assessment of its performance and transient behaviour is addressed in [12].

One such novel low-head pumped storage system aimed at coastal environments and shallow seas has been proposed [7,13]. At its core is an axial-flow reversible pump–turbine (RPT) consisting of two contra-rotating runners [14,15]. There are two fully separate drivetrains connecting each of these runners to their own electrical machine. The aim of utilising two independent runners is to achieve high efficiencies over the wider operating range, have more stable head-flow characteristic curves and achieve the desired power capacity with a more compact design — aiding faster power ramp rates and mode switching times, as reviewed in [12]. The development effort also includes dedicated grid and machine-side control with the goal to rapidly change between pump and turbine modes as well as quick adjustments of its power setpoints [16]. These technologies have been considered a promising solution for low-head applications, where discussions regarding the potential civil structures as well as legal and environmental concerns have also been addressed [13,17].

To understand the steady-state performance of the system over its operating range and its transient behaviour, crucial for the safe and dynamic operation of the system, both numerical and experimental methods can be employed [18]. Computational Fluid Dynamics (CFD) simulations and small-scale experimental testing can give reliable results, however, also have limitations. High-fidelity CFD models are a key tool when developing new hydro-machinery. They are capable of delivering accurate results on performance and predict complex flow patterns both in steady-state and for transient simulations [19]. Their major disadvantage is the computational expense, which can limit the size of the computational domain and transient effects that are included. Inherently, this leads to limitations in the amount of different operating conditions and cases that can be evaluated [20,21]. Additionally, CFD simulations focus on the flow behaviour and typically do not include other relevant system dynamics resulting from the interaction or coupling with the drivetrain, electrical machines or control subsystems. Experimental setups can provide reliable results for both steady-state and dynamic investigations but are costly, complex for the reduced scale fabrication of pump–turbine sets and time-consuming. Furthermore, they present challenges regarding accurate measurements, scaling issues and safety concerns among others. Using low and medium fidelity numerical approaches have the advantage of a drastic reduction in the computational resources required. Additionally, these versatile approaches allow for the integration of other system dynamics and control algorithms, enabling the simulation of a wide variety of scenarios. The trade-off of this efficiency and versatility is a decrease in accuracy compared to higher fidelity models. Nonetheless, if an appropriate modelling approach is chosen to consider all relevant effects to the desired simulation cases, adequate accuracy can be reached. Once verified, such a model can be applied to simulate the steady-state performance and transient behaviour of a full-scale storage plant.

This research presents, for the first time, experimental results of a newly developed pump–turbine technology for low-head pumped hydro storage applications and uses these results to benchmark a medium-fidelity numerical model. The presented 50 kW experimental setup features a 1:22 scaled model of said reversible pump–turbine, which, unlike conventional pump–turbine technologies, utilises two contra-rotating runners, each integrated into fully independent drivetrains. This unique configuration, which allows for individual variable speed control of each runner, enables a wide range of operating conditions. The experimental setup serves to benchmark both a steady-state pump–turbine model, based on a range of existing CFD simulations, and an extended medium-fidelity time-domain numerical model. The latter captures the dynamic behaviour of the main components, integrating the hydraulic conduits, the reversible pump–turbine, and the dual drivetrain system. The modelled RPT, utilising two independent runners, poses a novel challenge of modelling their interaction and coupling to the other system components. A series of steady-state and dynamic experiments are conducted, with their results compared against the numerical predictions. Benchmarking these numerical modelling approaches is a crucial step in the development of the technology for full-scale deployment. Lastly, the extended model is used to simulate transient dynamics during a shutdown sequence in turbine mode, offering new insights into operational behaviour.

Existing literature on low-head pumped hydro storage is limited to conceptual work and numerical investigations focusing on potential pump–turbines, i.e. [22–24]. Overall there is a lack of numerical evaluations of integrated low-head pumped storage systems as well as experimental testing of novel RPT technologies. Based on these gaps in the pertinent literature and the aforementioned motivation, the following specific objectives are guiding this work:

- Present an experimental setup comprising of two open surface tanks and incorporating a 1:22 scale reversible pump–turbine with two independent contra-rotating runners.
- Compare the experimental results of the reversible pump–turbine with the steady-state pump–turbine model based on existing high-fidelity CFD results.
- Develop and compare a medium fidelity dynamic model with experimental results for the transient response for a change of operating points.
- Apply the medium fidelity dynamic model to assess the risk of potential transient pressure effects for the experimental setup during a shutdown sequence.

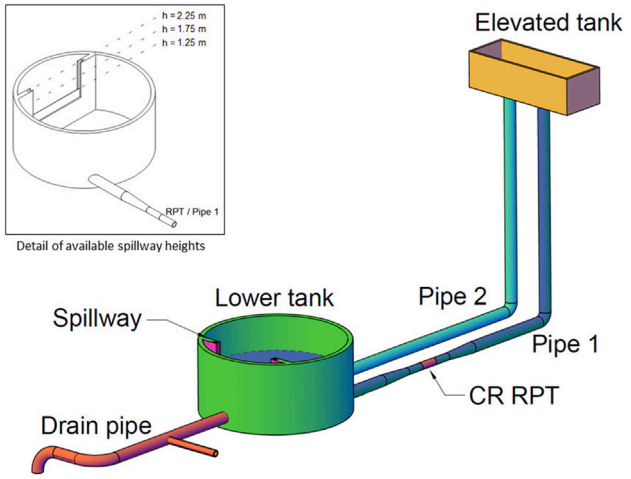



**Fig. 1.** Schematic overview of the experimental setup including the upper and lower reservoir, spillway, piping and contra-rotating RPT. The setup allows for testing net heads of 7.45 and 8.45 m, and volumetric flow rates up to 400 l/s.

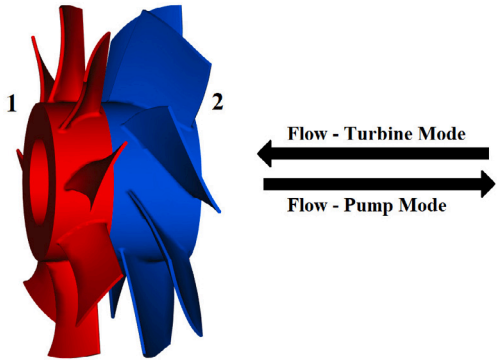



**Fig. 2.** Reversible pump–turbine with a diameter of 27.6 cm and a design flow rate of 283 l/s in turbine mode and 375 l/s in pump mode. Runner 1 is shown in red and runner 2 in blue. The arrows indicate the operating flow direction.

Following in Section 2, the experimental setup, methodology and instrumentation are presented before delving into the numerical approaches in Section 3. Subsequently, the results for the comparison of experimental and numerical results for the steady-state performance of the RPT are presented in Section 4.1. In Section 4.2, a change of operating point is simulated and compared to the corresponding experimental case. Section 5 shows the analysis of the turbine shutdown sequence. At last, the conclusions are given in Section 6.

## 2. Experimental setup and methods

### 2.1. Hydraulic facilities with open surface tanks

The experimental setup was constructed at the Leichtweiß-Institute for Hydraulic Engineering and Water Resources of the Technische Universität Braunschweig in Germany. Fig. 1 provides a schematic overview of the setup, which includes two open surface tanks [25]. The tanks model the upper and lower reservoir found in pumped hydro storage applications. The lower tank features an adjustable spillway and both tanks are connected via two pipes; the first incorporating the reduced scale contra-rotating reversible pump–turbine (CR-RPT). The water level of the elevated tank is 9.7 m above the centre line of the RPT, whereas the level in the lower tank is between 1.25 and 2.25 m above the centre line. This results in a gross head of the system between 7.45 and 8.45 m. The pipes have a diameter of 50 cm, tapering to 27.6 cm via two contraction/expansion sections which are designed at a 4-degree angle to prevent flow separation. This configuration allows for a maximum flow rate of approximately 400 l/s. A butterfly valve is positioned between the elevated tank and the RPT, with the aim to enable manual control of the discharge flow, nevertheless, it can also alter the net head over the RPT. The setup is designed to enable testing in both turbine and pump modes. In turbine mode, the flow goes from the elevated tank to the lower tank through the RPT in pipe 1, while pipe 2 remains closed. In pump mode, pipe 2 is opened, which allows a flow from the elevated tank to maintain a stable water level in the lower tank. In both modes, water is pumped from an underground reservoir to the elevated tank via the laboratory's supply system. The elevated tank is equipped with a sharp-edged weir to maintain a consistent water level when sufficiently supplied with water discharge. This ensures a constant static pressure throughout the experimental runs.

This experimental design is notable for its use of free surface tanks, solely relying on gravity to provide the required hydraulic head, distinguishing it from other pump–turbine test configurations that predominantly utilise pumps to achieve this [26,27]. The gravity-based system was chosen with the aim of reproducing more realistic in- and outflow conditions, assuming a reduced risk of swirl and pressure fluctuations typically induced by pump systems.

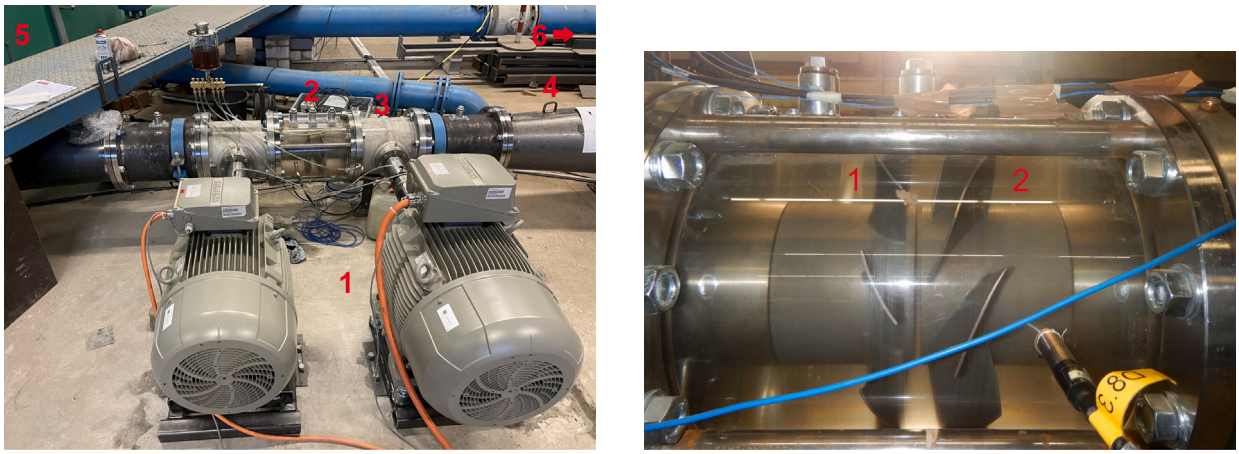
### 2.2. Contra-rotating reversible pump–turbine

The scaled 1:22 contra-rotating RPT is shown in Fig. 2. This RPT is a scaled version with geometric similarity of a 10 MW prototype with a diameter of 5.68 m [28]. Here, the affinity laws are applied to scale the RPT diameter so that the flow coefficient, head coefficient and power coefficient are equal in prototype and model scale [7]. Runner 1 is the downstream runner in turbine mode and is depicted in red. Consequently, runner 2 is downstream in pump mode, indicated in blue colour. In turbine and pump modes, runner 1 rotates clockwise and runner 2 counter-clockwise relative to their respective flow direction. The rotational speed of each runner can be controlled individually, resulting in an adjustable speed ratio between the runners, with the operating range encompassing ratios between 0.7 and 1.0. While runner 1 rotates faster for most of that range, runner 2 is designed with a larger axial length and consequently experiences larger torques. The additional degree of freedom emerging from the ability to control each of the runners individually means that for any given RPT net head, a variety of operating points can be achieved. In turbine mode, the RPT has a design flow rate of around 283 l/s and a design power of 16.7 kW, with an expected efficiency of 90.3%. In pump mode, the design flow rate is about 375 l/s with a power rating of 55.4 kW at an efficiency of 88.5% [29].

The runners are manufactured via 3D-printing using the aluminium alloy AlSi10Mg. After the printing process, both runners have undergone a process of vibratory finishing, reducing the surface roughness to 3.58 µm for runner 1 and 2.32 µm for runner 2. A smooth runner surface is desirable due to an improved hydraulic performance as well as a better comparison to CFD results which assume an ideal surface.

### 2.3. Drivetrain assembly

Each runner of the RPT is powered by a set of power-electronic drives and electrical machines rated for 37 kW each. To connect the runners to the electric machines, two sets of bevel gears are included in the hubs to either side of the RPT. Due to the diameter of these bevel gears being constrained by the inner hub diameter, the maximum torque of each drivetrain is limited to around 200 Nm. A photograph of the RPT and drivetrain assembly is shown in Fig. 3(a). In the lower part of the image, the two electric machines and their drive shafts leading to the bevel gears can be seen. The RPT is mounted in a transparent piece of pipe made of acrylic tube. This has the advantage that the physical integrity of the runners and potential cavitation can be visually




(a) (b)

**Fig. 3.** (a) Assembly of the RPT and drivetrains including the electrical machines (1), the RPT surrounded by an acrylic tube (2), hidden bevel gears (3), contraction and expansion tubes to either side (4), lower tank (5) and not visible flow meter, butterfly valve and elevated tank (6). (b) Close-up of the RPT, showing runner 1 to the left (1) and runner 2 to the right (2).

assessed. A drip feed lubricator is used to provide a constant flow of oil to the bevel gears and shaft seals. The out-flowing oil can be inspected for metal particles indicating excessive wear of the gears, which could be caused by the initial alignment of the drivetrain assembly having moved. The alignment of the electric machines, driveshafts, gears and runners is crucial to avoid such wear and the resultant friction torques but also to minimise vibrations. Additionally, the RPT was manufactured and assembled with a tip clearance of 0.5 mm, further necessitating very low tolerances on the whole assembly. Fig. 3(b) shows a close-up image of the RPT within its acrylic tube.

### 2.4. Instrumentation and data acquisition

The setup is equipped with a range of sensors to record data on the flow characteristics and machine operation. The instrumentation is listed in Table 1 and the location of the pressure probes and torque sensors illustrated in Fig. 4 [25]. The 12 pressure probes, denoted p1–12, are located in six different axial locations. For each of these locations, the values given by both probes are averaged. The difference between probes p7/p8 and p5/p6 is used to obtain the RPT net head. Additionally, probes are located just before (p3/4 and p9/10) and after (p1/2 and p11/12) the contraction and expansions tubes. An electromagnetic flow meter is located between the butterfly valve and the RPT. The electromagnetic flow meter was chosen due to its minimal disturbance of the flow. The torques are measured for each drivetrain using two torque transducers positioned next to the electrical machines. The variable frequency drives provide an estimation of the rotational speeds as well as the machine torques based on an internal machine model.

The setup is operated to perform both steady-state and dynamic tests. During steady-state tests, a sampling frequency of 10 Hz is selected and each steady-state point is measured over at least 60 s. Dynamic cases are recorded at 1000 Hz. To minimise the potential error on the pressure measurements, all probes are (re-)calibrated at a maximum of one week prior to the tests. To account for a potential drift in the measured pressure data in between probe calibrations, each testing day a static pressure measurement is conducted with all probes, allowing to correct with the known height of the water column relative to the position of the individual probes.

### 2.5. Testing protocol and operating range

There are two main limitations to be considered in this experimental setup. The first is the maximum torque caused by the limited diameter of the bevel gears. The second is the risk of cavitation due to the low hydraulic head at the low pressure side of the RPT. Within these limitations, a wide range of steady-state operating conditions have been tested with the experimental setup to evaluate the steady-state performance of the RPT. An overview of all tests is given in Table 2. In turbine mode, a total of 92 operating points have been tested. Since the rotational speed of each runner can be adjusted separately, tests are conducted incrementally across the whole speed range of each runner and for varying speed ratios ($\omega_2/\omega_1$) between them. Additional operating conditions were reached by closing the butterfly valve to an angle of 45° (half-closed) and 22.5° (three-quarters closed) as well as by adjusting the spillway, situated in the lower reservoir, to vary the net pressure head over the RPT. However, by reducing the height of the spillway to 1.25 m, and with that the static head on the low-pressure side of the RPT, significant cavitation was audibly and visually observed on the runners. Therefore, the number of cases under these conditions was limited to avoid damage to the pump–turbine. It was also observed that for rotational speeds below 500 RPM, flow separation occurred, rendering the pressure measurements of the probes directly downstream of the RPT unusable. Consequently, no reliable RPT net head could be obtained for these operating points. In pump mode, a total of 29 operating points were obtained. Pump mode testing is constrained due to several factors. Firstly, it is necessary to create a sufficient RPT net head to overcome the gross head, requiring a minimum rotational speed of both runners. Additionally, the torque limitations of the bevel gears limit the upper end of the operating range. For these reasons, the butterfly valve was not used in pump mode testing. Furthermore, akin to turbine mode testing, the risk of cavitation did not allow for a reduction in the spillway height.

To reach the desired operating points, start-up and shut-down sequences in turbine and pump modes must be carefully defined to ensure safe and reliable system operation. A key concern is the potential for a sudden and significant torque spike in the bevel gears during rapid transitions between operating conditions. In pump mode, it is also critical to prevent reverse flow, which can lead to operational instability and excessive pressure build-up. The start-up sequence has been optimised by Fahlbeck et al. [30].

In addition to the flow rate, the rotational speeds and the RPT net head measurements, the individual hydraulic torques of both runners are required to characterise the RPT behaviour under different operating conditions. Torque measurements for both drivetrains are taken outside of the RPT assembly, adjacent to their respective electric machines. This means that the measured torques include the friction torques, mainly induced by the bevel gears. These have to be accounted

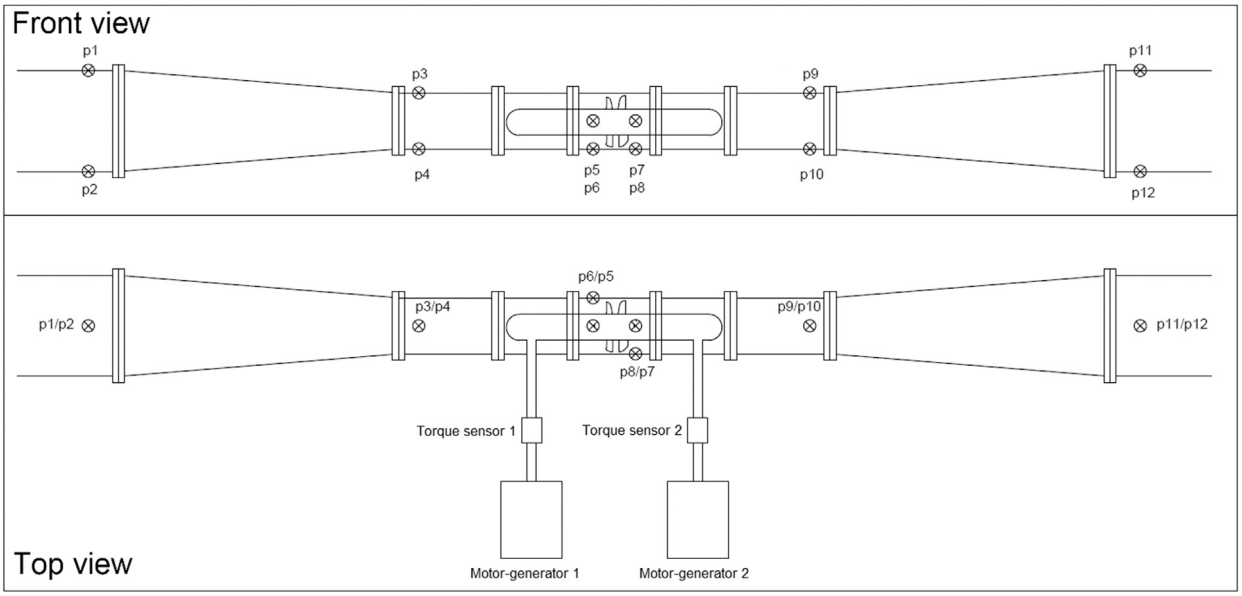



**Fig. 4.** Overview of the experimental setup instrumentation including 12 pressure probes (p1–12) and 2 torque sensors. Not depicted is an electromagnetic flow meter. Sketch not to scale.

**Table 1**
List of the used instrumentation.

| Measurement | Instrumentation | Type | Amount | Measurement range | Accuracy |
|---|---|---|---|---|---|
| Flow - $Q$ | Krohne OPTIFLUX 2000 | Electromagnetic flowmeter | 1 | 0–600 l/s | ±0.312% |
| Pressure - p1–6 | Druck Limited PDCR 1830 | Piezoresistive sensor | 6 | −0.5–0.35 bar | ±0.1% |
| Pressure - p7,9,10,12 | BD Sensors DMP 321 | Piezoresistive sensor | 4 | 0–2.4 bar | ±0.25% |
| Pressure - p8,11 | Druck Limited PDCR 830 | Piezoresistive sensor | 2 | −0.5–5 bar | ±0.1% |
| Torque - $\tau_{1,2}$ | HBM T22 | Strain gauge torque-transducer | 2 | 0–500 Nm | ±0.5% |
| Rotational Speed - $\omega_{1,2}$ | Siemens Sinamics S120 | Motor-Generator Drive | 2 | – | ±0.04% |

**Table 2**
Overview of steady-state experimental tests. A total of 121 operating points, 92 in turbine and 29 in pump mode, were recorded.

| Mode | $\omega_2/\omega_1$ | $\omega_1$ [RPM] | $\omega_2$ [RPM] | Valve Angle [deg] | Spillway Height [m] | Nr. of Points |
|---|---|---|---|---|---|---|
| Turbine | 1.000 | 100–1100 | 100–1100 | 90 | 2.7 | 15 |
| Turbine | 0.900 | 100–1100 | 90–990 | 90 | 2.7 | 12 |
| Turbine | 0.900 | 800–1100 | 720–990 | 90 | 1.7 | 4 |
| Turbine | 0.800 | 100–1100 | 80–880 | 90 | 2.7 | 13 |
| Turbine | 0.800 | 500–1100 | 400–880 | 90 | 1.7 | 7 |
| Turbine | 0.752 | 100–1100 | 75.2–827.2 | 90 | 2.7 | 13 |
| Turbine | 0.752 | 842 | 632 | 90 | 1.7 | 1 |
| Turbine | 0.752 | 500–1100 | 376–827.2 | 45 | 2.7 | 7 |
| Turbine | 0.752 | 300–900 | 225.6–678.8 | 22.5 | 2.7 | 7 |
| Turbine | 0.700 | 100–1100 | 70–770 | 90 | 2.7 | 13 |
| Pump | 1.000 | 950–1100 | 950–1100 | 90 | 2.7 | 4 |
| Pump | 0.900 | 1050–1250 | 945–1125 | 90 | 2.7 | 7 |
| Pump | 0.800 | 1050–1250 | 840–1000 | 90 | 2.7 | 6 |
| Pump | 0.752 | 1100–1337 | 827.2–1005 | 90 | 2.7 | 6 |
| Pump | 0.700 | 1146–1350 | 802–945 | 90 | 2.7 | 6 |
| | | | Total Number of Points: | | | **121** |

for to obtain the required hydraulic torques of the runners. Therefore, the friction torques between the instrumentation and the runners were characterised separately across the speed range of the runners. To gather the required data, the entire setup is drained and both runners incrementally accelerated in 100 RPM steps. At each step, the torque is recorded for a short period of time. In the absence of hydraulic forces, these measurements can be used to obtain the friction torques under steady-state conditions.

The torque measurements, used for the friction torque characterisation, were obtained from the power electronic drives instead of the

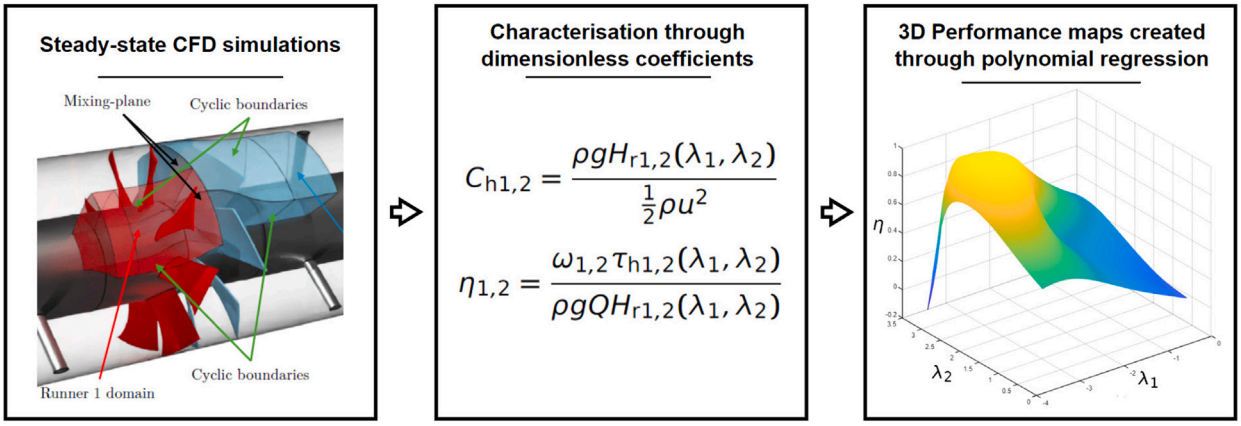



**Fig. 5.** Illustration showing the conversion of the steady-state CFD simulations to the RPT characterisation based on dimensionless coefficients.

dedicated torque sensors. The reason for this is that the measured friction torques are in the range of 1–6.5 Nm for runner 1 and 1–9.5 Nm for runner 2. This is within 2% of the measurement range of the torque meters (500 Nm), which increases the relative significance of noise and reduces the reliability of the results.

## 3. Numerical modelling approach

### 3.1. Steady-state RPT characterisation

The performance of the RPT is characterised based on 180 existing steady-state CFD simulations, according to Fahlbeck et al. [14], covering the full operating range in pump and turbine modes. The simulations used a 3-D computational domain representing a single blade passage per runner, assuming an infinite hub. The boundary conditions involved specifying the flow rate at the inlet (flowRateInletVelocity) and applying a static pressure at the outlet (fixedValue), with reversed flow restricted at the outlet using the inletOutlet condition. A no-slip condition was applied at the walls and wall functions were employed for turbulent quantities (k, $\omega$, $\nu$t) due to an average y+ of 5–10. The wall functions selected were kqRWallFunction, omegaWallFunction, and nutUSpaldingWallFunction, suitable for both low and high Reynolds number conditions. At the inlet, a turbulent intensity of 5% was assumed, with a mixing length applied based on the hydraulic diameter. The convection terms for momentum equations were discretised using a second-order accurate linear-upwind scheme, while the turbulent quantities (k, $\omega$) were treated with a first-order accurate upwind scheme. A segregated SIMPLE algorithm was used for pressure–velocity coupling, with under-relaxation factors of 0.6 for velocity, 0.4 for pressure, and 0.7 for turbulent quantities. A Preconditioned Bi-Conjugate Gradient Stabilized (PBiCGStab) solver was applied to all variables. The simulations were conducted using OpenFOAM v2306 with the simpleFoam solver, running for 3000 iterations. Final residuals were typically on the order of 1e−5 for velocity components, continuity, turbulent kinetic energy (k), and specific turbulence dissipation rate ($\omega$), while the pressure residual was around 1e−4.

The characterisation of the RPT is achieved by obtaining a set of dimensionless coefficients of the overall stage RPT net head and the hydraulic torques of each runner for all simulated data points, as given by:

$$C_{\mathrm{H}} = \frac{\rho g H_{\mathrm{RPT}}(\lambda_1, \lambda_2)}{\frac{1}{2}\rho u^2} \tag{1}$$

$$C_{\tau,i} = \frac{\tau_{\mathrm{h},i}(\lambda_1, \lambda_2)}{\frac{1}{2}\rho A R u^2} \tag{2}$$

Here, $C_{\mathrm{H}}$ is the head coefficient, which is a dimensionless parameter that represents the ratio of the net pressure head of the RPT to the dynamic pressure of the fluid. $\rho$ is the fluid density (kg/m$^3$), $g$ the gravitational acceleration (m/s$^2$) and $H_{\mathrm{RPT}}$ is the net RPT head (m), which is dependent on the tip speed ratios $\lambda_1$ and $\lambda_2$. The denominator, $\frac{1}{2}\rho u^2$, is the dynamic pressure (Pa), where $u$ is the average axial fluid velocity (m/s).

$C_{\tau,i}$ are the dimensionless hydraulic torque coefficients representing the ratio between each of the runners' hydraulic torques (Nm), $\tau_{\mathrm{h},i}$, and the available hydraulic reference torque. This coefficient allows for the independent assessment of the hydraulic performance of each runner. $A$ is the cross-sectional area of the RPT bladed area (m$^2$) and $R$ the RPT radius (m). The subindex $i$ is used to refer to either runner 1 or 2.

The tip speed ratios are defined as the tangential tip speed of the runners calculated from the rotational speeds $\omega_i$ (rad/s) and the runner radius divided by the average axial flow velocity as:

$$\lambda_i = \frac{\omega_i R}{u} \tag{3}$$

An equivalent alternative to the tip speed ratio is the flow coefficient which is more commonly used in literature regarding hydraulic machinery, where the flow coefficient can be expressed as the inverse of the tip speed ratio. The hydraulic efficiency of the RPT in turbine mode $\eta_{h,t}$, is defined as the ratio between the total mechanical power of the two runners and the available hydraulic power to the device:

$$\eta_{h,t} = \frac{\omega_1 \tau_{\mathrm{h},1} + \omega_2 \tau_{\mathrm{h},2}}{\rho g Q H_{\mathrm{RPT}}} \tag{4}$$

The mechanical power of each runner is given by the product of their respective rotational speed and hydraulic torque. While the available hydraulic power is given by the volumetric flow rate $Q$ (m$^3$/s), the fluid density, the gravitational acceleration and the RPT net head. The process of obtaining the RPT characterisation in the form of the 3-D maps from the CFD simulations is illustrated in Fig. 5. A non-linear polynomial regression is performed on the dimensionless coefficients using the tip speed ratios of both runners as the independent variables.

### 3.2. Integrated dynamic model

An integrated dynamic model is developed to assess system behaviour, taking into account the interaction effects between the runners of the RPT, the water conduits, the drivetrains and the valve actuator. In this study, the term dynamic model refers to a time-dependent representation of the system, capable of simulating how various physical quantities — such as flow rate, pressure head, and rotational speed — evolve in response to changes in operating conditions or control inputs. A similar model has been previously presented and implemented in [10]. A set of algebraic and ordinary differential equations (ODE) is used to describe the fully non-linear coupled model based on physical principles. The equations are implemented and solved numerically in

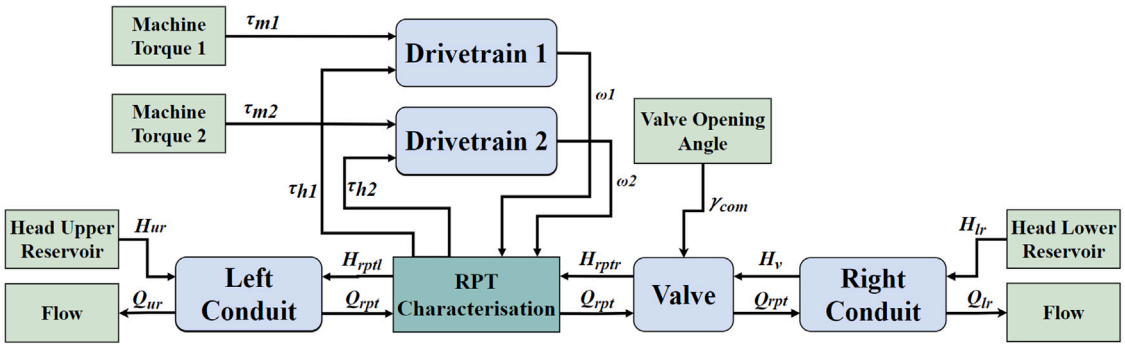



**Fig. 6.** Schematic overview of the system model, including the steady-state RPT model in dark green and dynamic components in blue. Inputs and outputs at the boundaries are shown in light green.

the time-domain using a standard ODE solver, following the so-called Method of Lines [31]. A schematic overview of the system model can be found in Fig. 6, where the coupling between the physical variables for each of the components is highlighted.

At the core of this integrated model is the steady-state RPT characterisation derived from the existing CFD results, as described in 3.1. The inputs of the RPT model are the runners' rotational speeds $\omega_{1,2}$ and the RPT flow rate $Q_{rpt}$. The outputs are the RPT net head and the hydraulic torques of both runners $\tau_{h1,2}$. The RPT model is coupled to the two individual drivetrains, to the valve actuator and to both sections of the conduit at either side of the RPT. The drivetrain models output the rotational speeds based on the hydraulic torques and the machine torques provided by the control setting. The control also inputs the valve opening angle command $\gamma_{com}$ to the valve actuator model. Finally, the heads at the upper and lower reservoir $H_{ur}$, $H_{lr}$ are fed into the two conduit sections, which output the flow rates to either side.

*Conduit model*

In order to numerically model the pipe sections of the setup, a 1-D approach considering the compressibility of water is used. This approach is chosen to cover potential transient pressure effects caused by the increased water inertia in low-head systems. This approach, modelling the change in pressure and flow along the water conduit, is based on the equations of conservation of mass and momentum [32–34]:

$$\frac{\partial H}{\partial t} = -\frac{a^2}{gA}\frac{\partial Q}{\partial x} \tag{5}$$

$$\frac{\partial Q}{\partial t} = -gA\frac{\partial H}{\partial x} - \frac{fQ|Q|}{2DA} - \frac{k_u}{g}\left[\frac{\partial Q}{\partial t} + \frac{Q}{|Q|}a\left|\frac{\partial Q}{\partial x}\right|\right] \tag{6}$$

Where $H$ is the pressure head (m), $a$ the pressure wave velocity in water (m/s) and $D$ the conduit diameter (m). Steady friction is included through the dimensionless Darcy friction factor, $f$, and unsteady friction through a one-coefficient, $k_u$ (m/s$^2$), model as per [35]. The model does not account for the structural response of the conduit, but compressibility effects are incorporated through the pressure wave velocity.

The partial differential equations given in Eqs. (5) and (6) are discretised in space and converted to ODEs. A central-schemed finite difference method is used for the discretisation, resulting into a set of coupled non-linear ODEs. The boundary conditions are developed using characteristic equations in order to allow for either the flow rate or pressure heads as inputs. Details on the boundary conditions are given in Appendix. Hydraulic losses outside the numerical domain, $H_{\mathrm{lmin}}$ (m), are included at the boundaries via dimensionless minor loss coefficients $k$ according to:

$$H_{\mathrm{lmin}} = k\frac{u^2}{2g} \tag{7}$$

*Drivetrain model*

The rotational speeds of the drivetrains are modelled individually using the equation of rotational motion for a single degree of freedom rigid body,

$$J_i\frac{\mathrm{d}\omega_i}{\mathrm{d}t} = \tau_{\mathrm{h},i}(\lambda_1,\lambda_2) - \tau_{\mathrm{m},i} - \tau_{\mathrm{f},i} \tag{8}$$

The dynamic response of both drivetrains is dependent on the balance between the hydraulic torques, obtained from the RPT model, the electrical machine torques $\tau_{\mathrm{m},i}$ (Nm) received from the control and the friction torques as well as the drivetrain inertias. Considering no flexibility in the drivetrain assembly, the entire mass of each drivetrain is lumped together, represented by equivalent mass moments of rotational inertia $J_i$ (kg m$^2$).

*Valve actuator*

The butterfly valve used in the experimental setup is implemented in the model via a minor hydraulic loss coefficient for the valve, $k_v$, as a function of its opening angle $\gamma$ (deg) as given in [29]:

$$k_{\mathrm{V}}(\gamma) = \exp(-4.2351\ln(\gamma) + 18.1149) \tag{9}$$

The relationship between loss coefficient and valve angle is shown in Fig. 7. An opening angle of 90° corresponds to a fully open valve and 0° to a fully closed one. The minimum opening angle is restricted to 2° to avoid numerical instability as the loss coefficient trends towards infinity.

The valve actuator response is modelled using a first-order linear ordinary differential equation,

$$\frac{\mathrm{d}\gamma}{\mathrm{d}t} = \frac{1}{T_{\mathrm{v}}}(\gamma_{\mathrm{com}} - \gamma) \tag{10}$$

with $\gamma_{\mathrm{com}}$ as the valve opening angle command (deg) and $T_{\mathrm{v}}$ as the valve time constant (s). The time constant allows to describe the time required by the actuator to follow the command angle.

## 4. Comparison of experimental results and numerical approaches

### 4.1. Steady-state results

*Friction torque characterisation*

The steady-state characterisation of the friction torques of each runner was performed through a regression analysis based on the dry friction test data as described in Section 2.5. Fig. 8 illustrates the range of the recorded raw data points at each rotational speed, their average and the corresponding regression curves for both runners. An empirical non-linear model was considered to give the most convenient representation of the friction torques $\tau_{\mathrm{f},i}$ (Nm) as a function of the rotational speeds according to:

$$\tau_{\mathrm{f},i} = B_i + C_i\omega_i^{D_i} \tag{11}$$

Here, $B_i$ are the static friction coefficients (Nm), $C_i$ the linear dynamic coefficients (N·m·s$^{D_i}$), $D_i$ the non-linear dynamic coefficients (-) and $\omega_i$ the rotational speed of either runner 1 or 2 (rad/s). For runner 1,

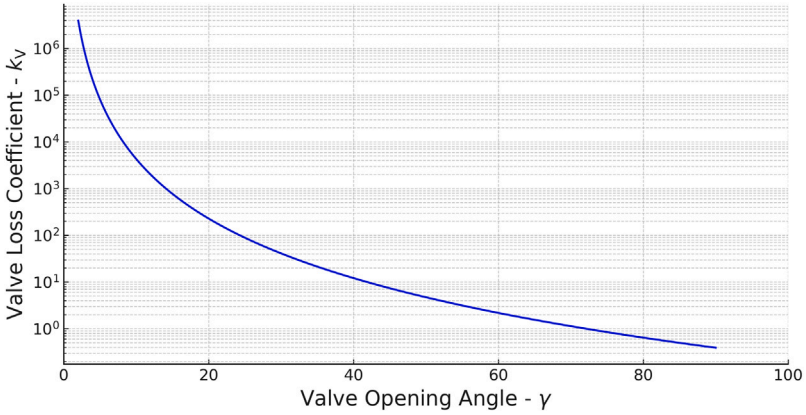



**Fig. 7.** Valve loss coefficient $k_v$ as a function of the valve opening angle $\gamma$.

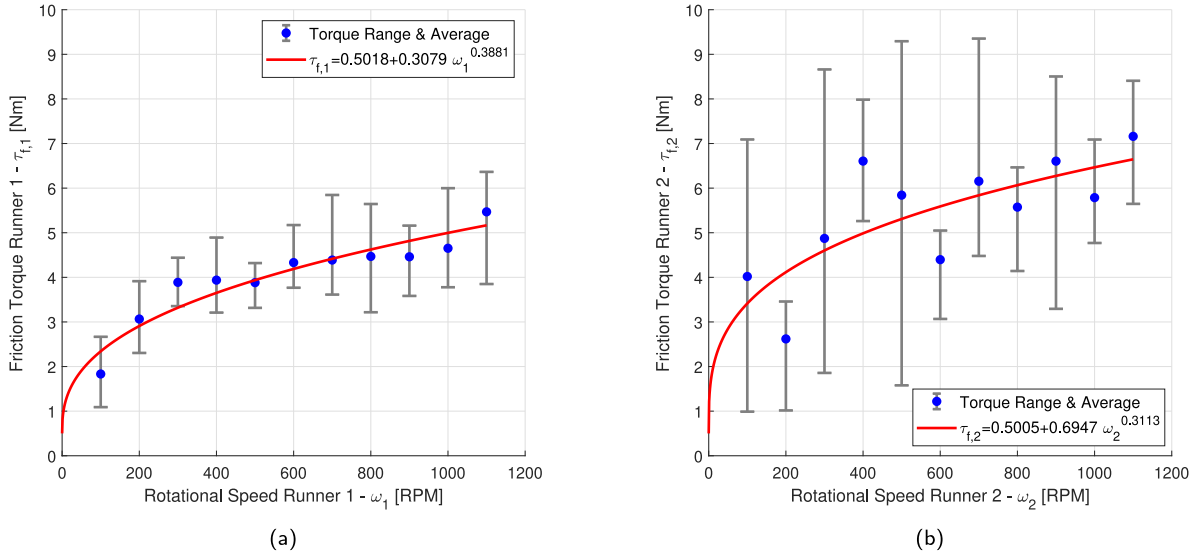



**Fig. 8.** Measured friction torques for runner 1 in (a) and runner 2 in (b) as well as their respective characteristic regression.

the spread of data for each rotational speed point is comparably low with the standard deviations ranging from 0.25 to 0.63 Nm for the individual rotational speeds. During the steady-state performance tests of the RPT, the torques for runner 1 range from a minimum of around 40 Nm to a maximum of 190 Nm. For the worst case scenario, applying the maximum deviation of the friction torque characterisation to the minimum torque, this leads to an error in the calculated hydraulic torques of below 4%. For runner 2, there is a much larger spread due to noise and inaccuracies in the torque approximations by the drives. The standard deviations here range from 0.35 to 2.88 Nm. The torque range of runner 2 during the experiments is between 60 Nm and 180 Nm. For the worst case, this may cause an error below 7%. While the average expected error is much lower, the resulting uncertainty must be considered when comparing the experimental and numerical results.

With the friction of both drivetrains characterised, the hydraulic torques of each runner are obtained by correcting the torques measured adjacent to the electric machines with the presented friction torque regression curves as a function of their rotational speed. In turbine mode, the respective friction torques are added to the measured torque and in pump mode subtracted.

*Comparison of experimental results and the RPT model*

During turbine mode testing, a maximum flow rate of 360 l/s was measured and a maximum mechanical power of 22 kW. The highest hydraulic efficiency measured during the experiments was 89%. In pump mode, a maximum flow rate of 370 l/s at a mechanical power of 42 kW was measured. The highest hydraulic efficiency measured in pump mode was 92%. The significant differences in mechanical power between turbine and pump mode arise from the hydraulic losses of the experimental setup. The hubs and struts adjacent to the RPT introduce considerable losses that reduce the generated power in turbine mode and increase the required power in pump mode. The maximum efficiencies between turbine and pump mode for the proposed RPT are comparable. However, efficiencies for RPTs generally differ between operating modes since the hydraulic geometry is typically designed and optimised for either turbine or pump operation. In turbine mode energy is extracted from the flow while in pump mode energy is introduced. This leads to differing flow characteristics which is a major challenge when designing a RPT capable of a high performance in both modes [27,36]. The contra-rotating RPT in this experimental setup has been designed specifically for pump mode, tested in turbine mode and then optimised for both [7]. At these best efficiency points, a hydraulic roundtrip efficiency of 82% is achieved. When accounting for additional hydraulic, mechanical, and conversion losses, this performance is still favourable compared to conventional pumped hydro storage plants, which commonly have roundtrip efficiencies ranging from 70% to 80% [37]. Alternative pumped storage concepts such as gravity energy storage, subsea storage or underground pumped storage are projected to achieve similar roundtrip efficiencies in the range of 70%–80% [38–40]. It should be noted though, that there are

scaling effects to be considered when using scaled-down experiments to evaluate the performance of full scale hydraulic machinery. These stem from differences in viscous effects, the geometry and general layout of the test setup as well as variations in the surface roughness compared to a full-scale power plant [41]. However, on-site measurements of full-scale plants are difficult and can be inaccurate [42]. Scaled-down experimental testing is therefore an efficient and useful tool to compare numerical and experimental results and use the numerical modelling approaches, once validated, to evaluate the performance of potential full-scale systems.

To compare the experimental results of the measured operating points with the steady-state RPT model, the experimental torque and head coefficients are calculated for all tested operating points. Based on the tip speed ratios of these operating points, the corresponding coefficients are obtained from the RPT model. Fig. 9 shows the comparison of the coefficients obtained experimentally and numerically in both turbine and pump operation.

Figs. 9(a), 9(c) and 9(e) show the comparison of experimental and numerical head and torque coefficients in turbine mode. For the head coefficient there is a very good match between experimental and numerical results with correlation coefficient values $R^2$ of 0.968. A minor trend, changing from a numerical to an experimental overestimation of the head coefficient as it increases can be observed. Generally, higher head coefficients correspond to the lower end of the rotational speed range of the runners. As previously discussed, at these lower speed operating points, flow separation starts to occur which affects the pressure measurements and with that the measured RPT net head. The effect of flow separation can be observed more clearly for the comparison of the torque coefficients for runner 1. While there still is an overall good match up until torque coefficients of about 0.95, above that, the compared points are less accurate. These higher torque coefficients similarly correspond to lower rotational speeds and tip speed ratios at which flow separation affects the hydraulic torque. Notably, this effect is only visible for runner 1 as it is the downstream runner in turbine mode. The observed flow separation was only present at operating points far from the design range of the RPT though and is therefore not significant for evaluating its overall performance. Leaving out the deviation towards the higher end of the torque coefficient, there is a minor overestimation of the numerical torques compared to the experimental results. The same can be observed for runner 2. Aside from potential inaccuracies in the CFD simulations, another likely cause may be an inaccuracy in the static component of the friction characterisation. However, with $R^2$-values of 0.898 and 0.934, the numerical model can still provide sufficient representation.

In pump mode, shown in Figs. 9(b), 9(d) and 9(f), the correlations are overall worse compared to turbine mode. For the head coefficients, a consistent constant offset of approximately 0.75 can be observed, although the slope of the correlation between experimental and numerical data remains accurate. Both comparisons of the torque coefficients in pump mode also show a worse correlation with both an offset and a linear deviation in the trend. Several factors likely contribute to these discrepancies between the numerical and experimental results. During the pump mode experiments, cavitation was observed throughout the operating range, which can lead to performance degradation in hydraulic machinery. This could explain the higher experimental torque values compared to the numerically predicted values needed to reach equivalent operating points. Additionally, the less accurate correlations in pump mode could be attributed to the proximity of RPT to the water inlet. In turbine mode, the flow reaches the RPT after a long straight section and the downwards pipe which reduces the risk of significant non-axial flow components being present. In contrast, the flow in pump mode may be more prone to disturbances due to the shorter upstream length. The CFD simulations, which assume uniform inflow conditions and use a relatively short computational domain, may not fully capture these non-uniformities in the experimental setup. This could cause discrepancies between the simulated and experimental flow behaviour. Although the friction torque characterisation might introduce inaccuracies, these should affect both turbine and pump modes similarly and therefore it is unlikely that friction alone can account for the mismatch observed in pump mode. Finally, the proximity of the pressure probes to the RPT could introduce errors in measuring the experimental RPT head values.

**Table 3**
Overview of simulation parameters used in the integrated system model.

| | | | |
|---|---|---|---|
| Conduit length | $L$ | 19.85 | m |
| Conduit diameter at RPT section | $D_1$ | 27.6 | cm |
| Conduit diameter piping | $D_2$ | 50 | cm |
| Pressure wave velocity | $a$ | 1000 | m/s |
| Darcy friction factor | $f$ | 0.0127 | – |
| Unsteady loss coefficient | $k$ | 0.04 | $m/s^2$ |
| Rotational inertia drivetrain 1 | $J_1$ | 0.116 | kg $m^2$ |
| Rotational inertia drivetrain 2 | $J_2$ | 0.145 | kg $m^2$ |
| **Minor loss coefficients** | | | |
| - Entrance | $k_{en}$ | 0.45 | – |
| - Exit | $k_{ex}$ | 1.0 | – |
| - Bend | $k_{be}$ | 0.2 | – |
| - Bulbs (incl. expansion/contraction) | $k_b$ | 2 × 5.21 | – |
| - Butterfly valve (fully open) | $k_v$ | 0.39 | – |
| - Safety valve (fully open) | $k_{v2}$ | 0.4 | – |

### 4.2. Comparison of dynamic results with the integrated system model

To evaluate the transient response of the system and benchmark the dynamic components of the numerical modelling approach, notably the hydraulic conduit and drivetrains, dynamic cases have also been tested with the experimental setup. The dynamic response of the flow rate is mainly driven by the balance between gross head, RPT net head and head losses of the experimental setup as well as the conduit water inertia. This inertia is defined by the dimensions of the conduit. Similarly, the dynamic response of the drivetrain is determined by the balance between the torques and the rotational mass moments of inertia of the individual drivetrains. To obtain accurate values for the rotational inertias of both drivetrains in the experimental setup, a characterisation test is performed. Both runners are accelerated in dry conditions to their maximum operating rotational speeds and then both motor torques are set to zero. Setting the hydraulic and generator torques in Eq. (8) to zero, the inertias are calculated based on the characterised friction torques and the change in rotational speed over time. Both inertias and all other relevant system parameters used in the simulations are given in Table 3. The geometric parameters were obtained from measurements of the laboratory setup. The pressure wave velocity, steady and unsteady friction factors are based on common estimates from literature [34,35]. The minor loss coefficients are either taken from [43] or obtained from CFD simulations, i.e. the bulbs including the expansion and contraction tubes.

The dynamic case chosen for the model validation starts in steady-state with runner 1 at 764 RPM (80 rad/s) and runner 2 at 611 RPM (64 rad/s). Both runners are then accelerated over the course of about one second to 1250 RPM (131 rad/s) and 1062.5 RPM (111 rad/s) respectively. Finally, both runners are decelerated to their original operating points. The valve remains fully open during the sequence. To simulate this case with the numerical model, the measured generator torques of both drivetrains are used as inputs to the drivetrain model. Additionally, the pressures recorded just outside the contraction and expansion tubes (see probes p1/2 and p11/12 in Fig. 4) are used as inputs to the boundaries of the computational domain. The corresponding generator torques are shown in Fig. 10. A moving average filter with a window size of 0.1 s has been applied to the data series.

At the timestep $t$ = 21 s, both generator torques are rapidly reduced to achieve the desired acceleration of the runners before increasing again to stabilise the rotational speeds at the new operating point. At $t$ = 41 s, the reverse happens to decelerate the runners back to their

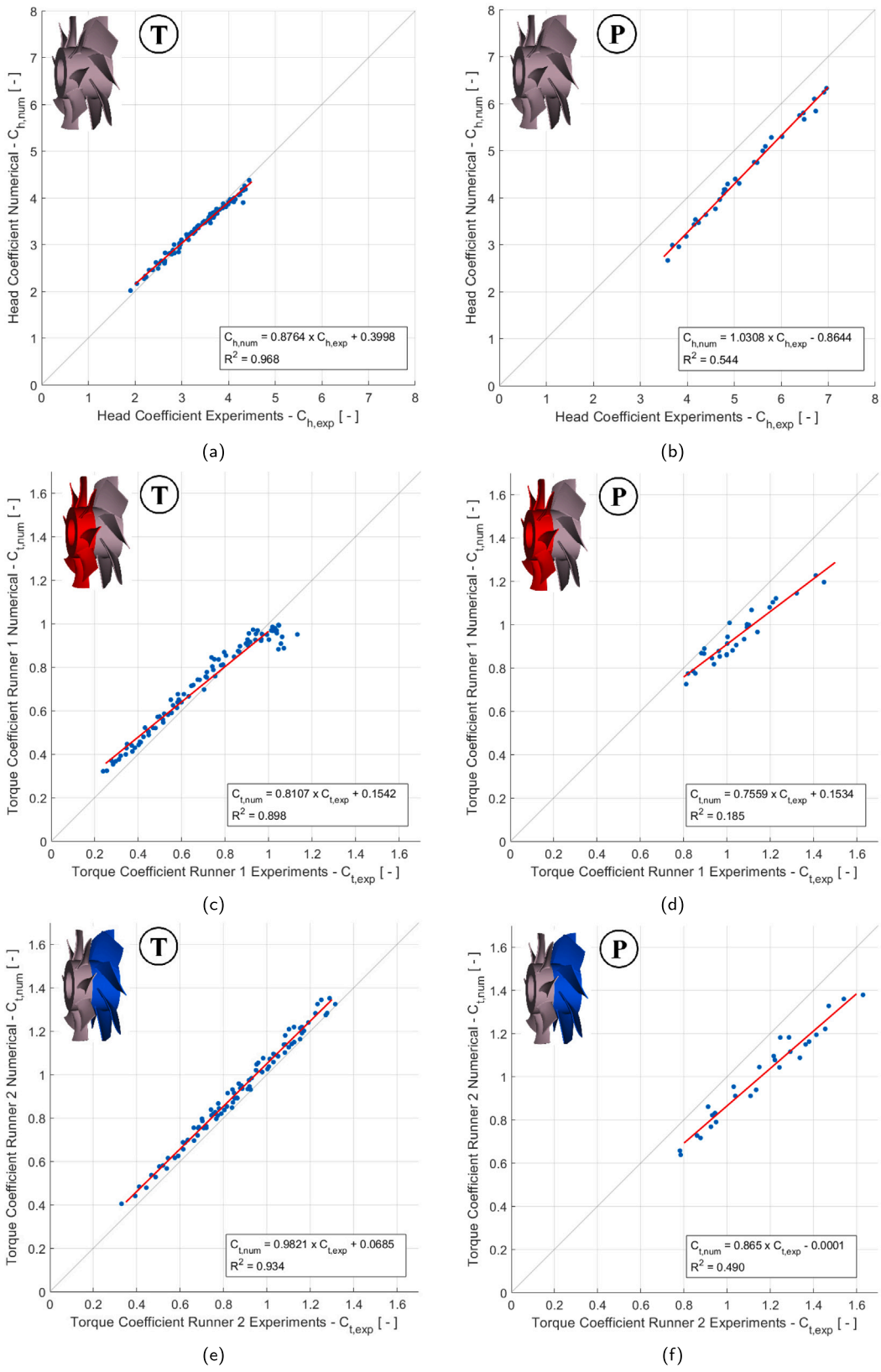



**Fig. 9.** Comparison of the steady-state head and torque coefficients of the experimental and numerical results. Turbine and pump operation are depicted with a *T* and P respectively, while runner 1 is in red and runner 2 is in blue.

original operating point. The resulting rotational speeds of runner 1 and 2 in the experimental test ($\omega_{1,Exp}$, $\omega_{2,Exp}$) and the simulation results ($\omega_{1,Sim}$, $\omega_{2,Sim}$) are shown in Fig. 11.

In order to focus on the validation of the dynamics, the friction torque coefficients were tuned in the numerical model to have the same conditions in steady-state for both rotational speeds. In steady-state

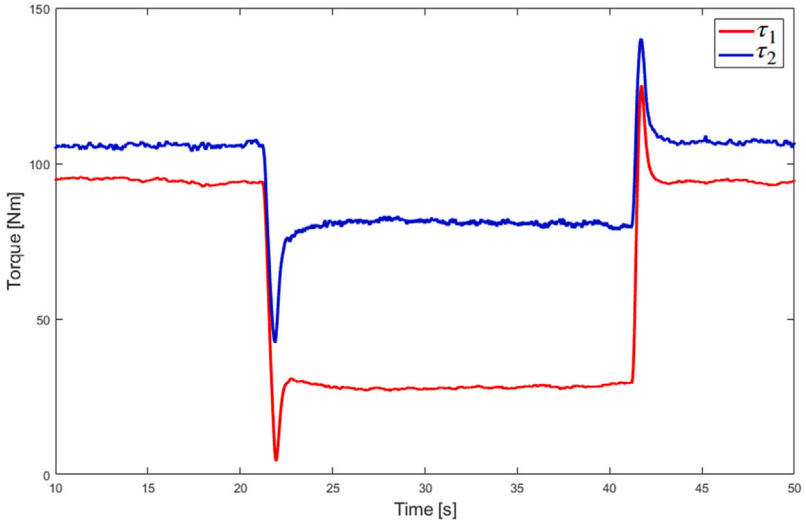



**Fig. 10.** Measured generator torques of both drivetrains during change of operating point. These values are used as an input to the simulation of the dynamic case.

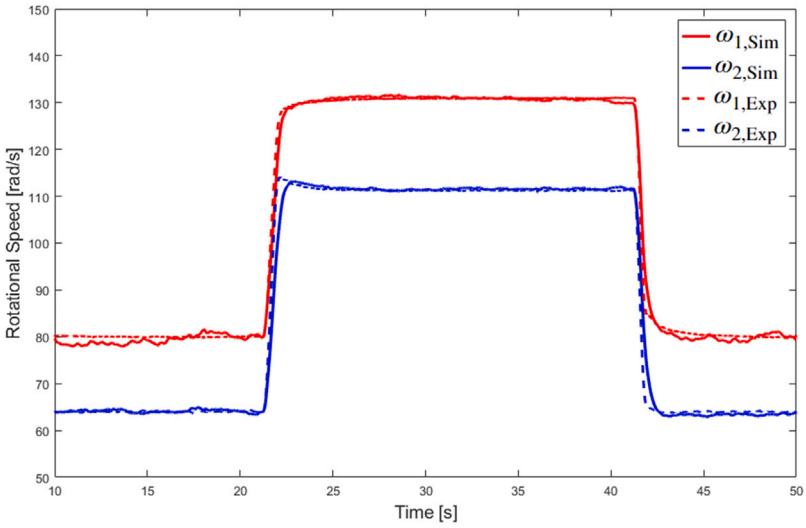



**Fig. 11.** Comparison of the rotational speeds of both runners during the experimental test and the change of operating point simulation.

conditions, minor deviations in the simulation results can be observed compared to the experimental results. The rotational speeds in the experiments are kept constant by the control algorithm of the drives, which adjusts the generator torques in response to load fluctuations caused by the turbulent flow around the hubs and struts adjacent to the RPT. These complex flow patterns are not captured in the 1-D modelling approach, resulting in the slight variations of rotational speeds. The dynamic response of the rotational speeds to the changes in generator torques show a close match between experiment and simulation. For both runners, a slightly slower response can be observed in the simulation. This indicates that the drivetrain inertias are marginally overestimated, likely caused by the uncertainty on the friction torque characterisation that is used to calculate the inertias of the drivetrains in the experimental setup.

The results for the flow rate of the experiment ($Q_{Exp}$) and simulation ($Q_{Sim}$) are shown in Fig. 12. At both operating points the steady-state values are closely matched with a difference at the higher operating point of $< 3\%$, reflecting the close match of the steady-state RPT model with the experimental results. The remaining difference is likely caused by a minor overestimation of the hydraulic losses. The dynamic response also shows the simulated flow reacting slightly faster than the experimental one. It is important to mention that the electromagnetic flow meter used to record the data uses a filter with a time constant of 0.1 s which effect also contributes to the slower response shown in the experimental data.

Overall, both major dynamic components of the numerical model show a close match compared to the experimental results. With the numerical approach partially validated, the model can be applied to a full scale system in order to simulate its dynamic behaviour when rapidly changing operating points. These changes in operating points correspond to adjusting its power setpoints and with that its capability to react so sudden grid demand fluctuations by providing frequency regulation services.

## 5. Turbine shutdown sequence simulation

Aside from changing its power setpoints, changing quickly between turbine and pump modes also improves the storage systems ability to react to changes in supply and demand of the grid. Such a mode switching sequence involves the deceleration and acceleration of both runners, reverting their direction of rotation and the closure and opening of the flow control valve. As previously discussed, low-head systems have an increased conduit inertia compared to conventional high-head system of the same power rating and are therefore at higher risk of

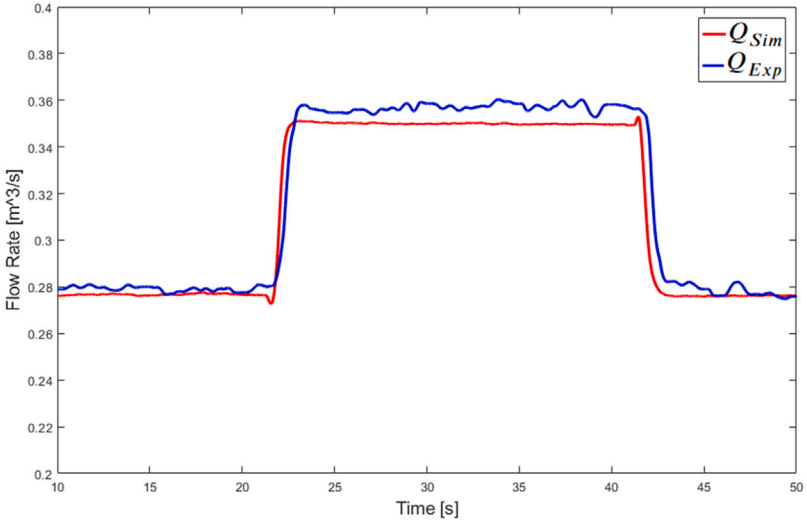



**Fig. 12.** Comparison of the volumetric flow rate during the experimental test and the change of operating point simulation.

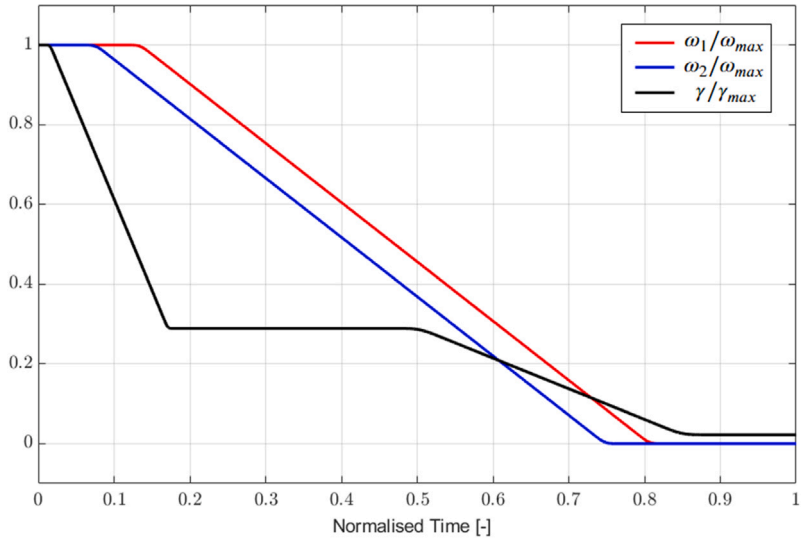



**Fig. 13.** Shutdown sequence in turbine mode including the rotational speeds of both runners and the valve opening angle.

transient pressure effects, commonly known as water hammer. For the 1:22 scaled version of the storage system in the laboratory, a mode switching sequence has been selected. However, due to safety concerns regarding potential pressure spikes during valve closure, this sequence cannot be tested at the desired speed. The highest risk of water hammer occurs during shutdown in turbine mode, as the largest amount of water is decelerated by the valve. To evaluate the potential pressure spikes, this shutdown sequence is simulated at different rates of runner deceleration and valve closure. The selected shutdown sequence is shown in Fig. 13.

The rotational speeds and the valve opening angle are normalised with their respective maximum values. The initial rotational speed of runner 1 is 842 RPM (~88 rad/s) and for runner 2 it is 633 RPM (~66 rad/s). This corresponds to a flow rate of 273 l/s. The time is also normalised with respect to the desired shutdown time for the whole sequence of 1.7 s. The valve is closed in two steps, starting just before both runners are decelerated and finishing after the runners are standing still. These rotational speeds and the valve opening angle are used as inputs to the numerical model. All other parameters remain unchanged as per the simulation carried out in Section 4.2. Since the experimental values of the pressures at the boundaries are not available, both upstream and downstream pipe sections are included in the computational model to account for the entire inertia of the water column. The sequence is simulated using its desired shutdown time as well as accelerated by a factor of 2, 4 and 10. The resulting pressure transients adjacent to the valve for these simulations are shown in Fig. 14.

The pressure head results of all simulations have been non-dimensionalised by dividing them by the expected static head, which in this case is 9.7 m. The initial two-thirds closure of the valve only results in a minor increase in pressure for all simulations. The major pressure fluctuations occur when the valve approaches full closure. At the desired sequence time, the simulation shows that the maximum pressure reaches roughly twice the static pressure. When doubling the rate of change, the maximum pressure reaches around four times the static pressure. Similarly, at four and ten times the rate of change, the pressure fluctuations have the potential to go up to eight and twenty-two times the static pressure respectively. At the desired rate of change and even at double the speed, the maximum pressure does not appear to pose a risk to the system. Depending on the specification of the conduit

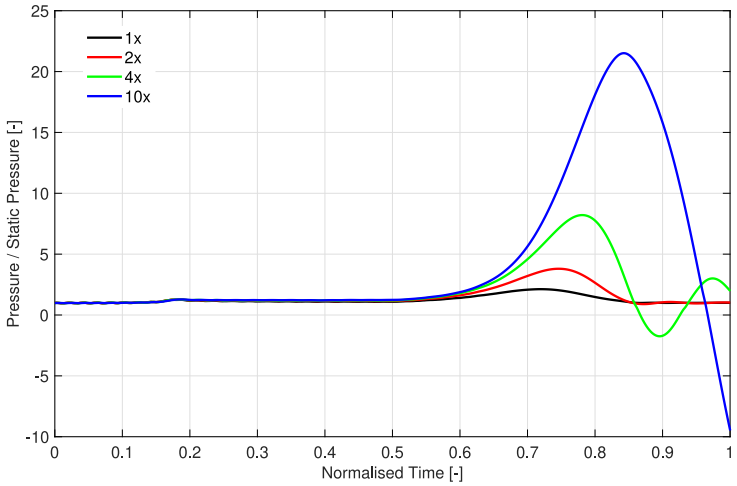



**Fig. 14.** Pressure adjacent to the valve for the shutdown sequence at original rate of change as well as accelerated by a factor of 2, 4 and 10.

and adjacent equipment, at higher rates, the maximum pressure may cause a risk to the integrity of the system. Additionally, at four and ten times the rate of change, a significant non-physical negative pressure transient can be observed following the positive spike and consequent reversing of the flow. This indicates column separation as the vapour pressure of water is reached, which may lead to damage to the conduit and equipment or even catastrophic failure.

## 6. Conclusion

An increased penetration of renewable energy generators into our power grids introduces significant intermittency and variability to our power supply, requiring large scale energy storage systems. Additionally, this increase in inverter coupled renewable energy sources also reduces the grid inertia and with that its stability. Energy storage systems are therefore required to aid this stability by rapidly changing its power output or input and switching between storage and generation modes. Low-head pumped hydro storage technology has the potential to contribute to grid-scale energy storage in countries that do not have the required topography to implement conventional high-head systems. Due to its differing operational characteristics, new innovative hardware and control approaches are required to maximise its capability to perform load shifting and frequency regulation services. Such new technology needs to be evaluated for its steady-state and dynamic performance. A 50 kW experimental setup incorporating a 1:22 scaled version of a new contra-rotating RPT has been constructed and used to perform steady-state and dynamic tests. The experimental results are compared to a numerical modelling approach.

Chapter 2 described the 50 kW laboratory-scale facility developed for this study, featuring open-surface tanks and a 1:22 scale CR-RPT. Details were provided on the hydraulic layout, the independently controlled dual-runner assembly, drivetrain integration, instrumentation, and the testing protocol. The section also presented the range of operating conditions tested in both turbine and pump modes and explained the friction torque characterisation necessary for accurate performance measurements.

In the following chapter 3 two modelling approaches were developed - a steady-state RPT model based on CFD-derived performance maps and the extended medium-fidelity integrated dynamic model. The steady-state model used dimensionless coefficients to characterise hydraulic head and torque across a wide operating range. The dynamic model integrated the dynamics of the conduit, drivetrains, and valve to simulate transient behaviour. Model structure, governing equations, and parameter selection were explained.

The comparison of numerical modelling and experimental results was given in chapter 4. The steady-state model shows a close match to the experimental results in turbine mode, with slightly worse results in pump mode. Challenges and uncertainties in this comparison arise for once from cavitation and flow separation affecting the pressure measurements close to the RPT. The effect of flow separation was only observed in far off-design operating conditions though and would not affect the performance of a full-scale system. Cavitation can lead to performance degradation for both the scaled-down and full-scale version of the technology. Full-scale systems would experience a larger static head at the low-pressure side of the RPT therefore reducing the risk of cavitation occurring. Nonetheless, this effect needs to be carefully evaluated before deployment. Further inaccuracies in the comparison may stem from the 3D CFD simulations that were used as a basis for the RPT characterisation. The proximity of the RPT to the inlet in pump mode introduced non-axial flow conditions that are not captured in the simulations due to the boundary conditions assuming a purely axial flow. Lastly, the placement of the torque transducers next to the electric machines instead of the RPT require the characterisation of the friction torques to obtain the hydraulic torques. To benchmark the dynamic modelling approach, a change of operating point has been tested and simulated in turbine mode. A close match between the dynamic response for both the rotational speeds and flow rate has been observed. Overall, the developed numerical approach has proven to provide accurate results for both steady-state and dynamic performance predictions.

Using the tested model, chapter 5 simulated a shutdown scenario in turbine mode to evaluate the risk of water hammer and pressure transients. The simulation confirmed that under the intended deceleration and valve closure rates, the system remained within safe pressure limits. However, it also revealed that faster shutdowns could induce dangerous transients and even column separation, underscoring the importance of properly managed control sequences in full-scale systems.

When assessing the performance of hydraulic machinery in scaled-down systems, uncertainties regarding the direct applicability of results to full-scale operations arise due to scaling effects. Despite these limitations, scaled experiments play a critical role in validating numerical models, which can then be reliably applied to full-scale systems. These validated models enable detailed evaluations of real-world applications. Future work should focus on integrating the verified numerical model with control algorithms to simulate full-scale system performance under realistic operating conditions. Such an approach will allow for comprehensive evaluations of energy balancing and frequency regulation services, further advancing the development of low-head pumped hydro storage technology.

## CRediT authorship contribution statement

**J.P. Hoffstaedt:** Writing – review & editing, Writing – original draft, Visualization, Validation, Software, Methodology, Investigation,

Formal analysis, Data curation, Conceptualization. **A. Jarquin Laguna:** Writing – review & editing, Writing – original draft, Supervision, Methodology, Investigation, Formal analysis, Conceptualization. **R. Ansorena Ruiz:** Writing – review & editing, Validation, Investigation, Formal analysis, Data curation. **D. Schürenkamp:** Writing – review & editing, Investigation. **N. Goseberg:** Writing – review & editing, Supervision. **D.P.K. Truijen:** Writing – review & editing, Validation, Investigation, Formal analysis, Data curation. **J.D.M. De Kooning:** Writing – review & editing, Supervision. **K. Stockman:** Supervision. **J. Fahlbeck:** Writing – review & editing, Resources. **H. Nilsson:** Writing – review & editing, Supervision, Resources.

## Declaration of competing interest

The authors declare the following financial interests/personal relationships which may be considered as potential competing interests: Justus Hoffstaedt reports financial support was provided by European Commission. Antonio Laguna reports financial support was provided by European Commission. Ruben Ansorena Ruiz reports financial support was provided by European Commission. David Schuerenkamp reports financial support was provided by European Commission. Nils Goseberg reports financial support was provided by European Commission. Daan Truijen reports financial support was provided by European Commission. Jeroen De Kooning reports financial support was provided by European Commission. Jonathan Fahlbeck reports financial support was provided by European Commission. Hakan Nilsson reports financial support was provided by European Commission. If there are other authors, they declare that they have no known competing financial interests or personal relationships that could have appeared to influence the work reported in this paper.

## Acknowledgements

This research is part of the ALPHEUS project, which has received funding from the European Union's Horizon 2020 research and innovation programme under grant agreement No. 883553. The CFD computations were enabled by resources provided by the National Academic Infrastructure for Supercomputing in Sweden (NAISS) at NSC and C3SE, partially funded by the Swedish Research Council through grant agreement No. 2022-06725.

## Appendix. Boundary conditions

To evaluate the pressure head and flow rate at the upstream and downstream ends of the computational domain, the method of characteristics is employed. This approach transforms the governing partial differential equations into algebraic expressions that relate pressure head and flow rate at boundary points. The characteristic equations applied at the upstream and downstream boundaries are shown in Eq. (12) and Eq. (13), respectively, following the formulation described by Chaudhry [35].

$$Q_{i,j} = Q_{i,j+1} - \frac{gA}{a} H_{i,j+1} - \frac{f}{2DA} \Delta t \, Q_{i,j+1} \left| Q_{i,j+1} \right| + \frac{gA}{a} H_{i,j} \tag{12}$$

$$Q_{i,j} = Q_{i,j-1} + \frac{gA}{a} H_{i,j-1} - \frac{f}{2DA} \Delta t \, Q_{i,j-1} \left| Q_{i,j-1} \right| - \frac{gA}{a} H_{i,j} \tag{13}$$

## Data availability

Data will be made available on request.

## References

[1] Qudaih M, Engel B, Truijen DPK, De Kooning JDM, Stockman K, Hoffstaedt JP, Jarquin-Laguna A, Ansorena Ruiz R, Goseberg N, de Vilder L, Bricker JD, Joseph M, Zangeneh M, Terheiden K. The contribution of low-head pumped hydro storage to grid stability in future power systems. IET Renew Power Gener 2022;1–15. http://dx.doi.org/10.1049/RPG2.12668.

[2] Ahmed F, Al Kez D, McLoone S, Best RJ, Cameron C, Foley A. Dynamic grid stability in low carbon power systems with minimum inertia. Renew Energy 2023;210:486–506. http://dx.doi.org/10.1016/j.renene.2023.03.082, https://www.sciencedirect.com/science/article/pii/S0960148123003774.

[3] Gür TM. Review of electrical energy storage technologies, materials and systems: challenges and prospects for large-scale grid storage. Energy & Environ Sci 2018;11(10):2696–767.

[4] Mongird K, Fotedar V, Viswanathan V, Koritarov V, Balducci P, Hadjerioua B, Alam J. Energy Storage Technology and Cost Characterization Report. Pacific Northwest National Laboratory (PNNL), Richland, WA (United States); 2019.

[5] Blakers A, Stocks M, Lu B, Cheng C. A review of pumped hydro energy storage. Prog Energy 2021;3(2). http://dx.doi.org/10.1088/2516-1083/abeb5b.

[6] Ren J, Ren X. Sustainability ranking of energy storage technologies under uncertainties. J Clean Prod 2018;170:1387–98. http://dx.doi.org/10.1016/j.jclepro.2017.09.229.

[7] Prasasti E, Aouad M, Joseph M, Zangeneh M, Terheiden K. Optimization of pumped hydro energy storage design and operation for offshore low-head application and grid stabilization. Renew Sustain Energy Rev 2024;191:114122.

[8] Ghidaoui MS, Zhao M, McInnis DA, Axworthy DH. A review of water hammer theory and practice. Appl Mech Rev 2005;58(1):49–76. http://dx.doi.org/10.1115/1.1828050, arXiv:https://asmedigitalcollection.asme.org/appliedmechanicsreviews/article-pdf/58/1/49/5440913/49_1.pdf.

[9] Kan K, Binama M, Chen H, Zheng Y, Zhou D, Su W, Muhirwa A. Pump as turbine cavitation performance for both conventional and reverse operating modes: A review. Renew Sustain Energy Rev 2022;168:112786.

[10] Hoffstaedt JP, Jarquín-Laguna A, Fahlbeck J, Nilsson H. System model development and numerical simulation of low-head pumped hydro storage. In: Trends in renewable energies offshore. 2022, p. 757–63. http://dx.doi.org/10.1201/9781003360773-85.

[11] Bader KB. The effect of static pressure on the inertial cavitation threshold and bubble collapse strength. In: ProQuest Dissertations and Theses (Ph.D. thesis), The University of Mississippi PP - United States – Mississippi; 2011, p. 239.

[12] Hoffstaedt JP, Truijen DPK, Fahlbeck J, Gans LHA, Qudaih M, Laguna AJ, De Kooning JDM, Stockman K, Nilsson H, Storli P-T, Engel B, Marence M, Bricker JD. Low-head pumped hydro storage: A review of applicable technologies for design, grid integration, control and modelling. Renew Sustain Energy Rev 2022;158:112119. http://dx.doi.org/10.1016/j.rser.2022.112119, https://www.sciencedirect.com/science/article/pii/S1364032122000478.

[13] Ansorena Ruiz R, de Vilder L, Prasasti E, Aouad M, De Luca A, Geisseler B, Terheiden K, Scanu S, Miccoli A, Roeber V, Marence M, Moll R, Bricker J, Goseberg N. Low-head pumped hydro storage: A review on civil structure designs, legal and environmental aspects to make its realization feasible in seawater. Renew Sustain Energy Rev 2022;160:112281. http://dx.doi.org/10.1016/j.rser.2022.112281, https://www.sciencedirect.com/science/article/pii/S1364032122002003.

[14] Fahlbeck J, Nilsson Ha, Salehi S, Zangeneh M, Joseph M. Numerical analysis of an initial design of a counter-rotating pump-turbine. IOP Conf Ser: Earth Environ Sci 2021;774(1):12066. http://dx.doi.org/10.1088/1755-1315/774/1/012066.

[15] Prasasti E, Joseph M, Miao X, Zangeneh M, Terheiden K. Design of shaft-and rim-driven contra-rotating reversible pump-turbine to optimize novel low-head pumped hydro energy storages. Energy 2024;306:132237.

[16] Truijen DP, Hoffstaedt JP, Fahlbeck J, Laguna AJ, Nilsson H, Stockman K, De Kooning JD. Impact of dual variable speed and inlet valve control on the efficiency and operating range of low-head contra-rotating pump-turbines. IEEE Access 2024.

[17] Miccoli A, De Luca A, Bricker J, Vriese FT, Moll R, Scapigliati G. Stress response to entrainment flow speed near pump inlet fish screens in two model teleost species, anguilla anguilla and oncorhynchus mykiss. Fishes 2023;8(3). http://dx.doi.org/10.3390/fishes8030139, https://www.mdpi.com/2410-3888/8/3/139.

[18] Hu J, Yang J, Zeng W, Yang J. Transient pressure analysis of a prototype pump turbine: Field tests and simulation. J Fluids Eng 2018;140(7):071102. http://dx.doi.org/10.1115/1.4039258.

[19] Tiwari G, Kumar J, Prasad V, Patel VK. Utility of CFD in the design and performance analysis of hydraulic turbines — A review. Energy Rep 2020;6:2410–29. http://dx.doi.org/10.1016/j.egyr.2020.09.004, https://www.sciencedirect.com/science/article/pii/S2352484720312920.

[20] Casartelli E, Del Rio A, Mangani L, Schmid A. Capturing the S-shape of pump-turbines by computational fluid dynamics simulations using an anisotropic turbulence model. J Fluids Eng 2021;144(2):021203. http://dx.doi.org/10.1115/1.4051809.

[21] Mrope HA, Chande Jande YA, Kivevele TT. A review on computational fluid dynamics applications in the design and optimization of crossflow hydro turbines. J Renew Energy 2021;1–13. http://dx.doi.org/10.1155/2021/5570848.

[22] Wang H, Wang F, Wang C, Wang B, Li C, Li D. A prospective assessment of scale effects of energy conversion in ultra-low-head pumped hydro energy storage units. Energy Convers Manage 2024;315:118798. http://dx.doi.org/10.1016/j.enconman.2024.118798, https://www.sciencedirect.com/science/article/pii/S0196890424007398.

[23] Shen J, Pei J, Wang W, Yuan S. Instability characteristics regarding the saddle-shaped region in a reversible mixed-flow pump applied to the low-head pumped storage. J Energy Storage 2023;63:107035. http://dx.doi.org/10.1016/j.est.2023.107035, https://www.sciencedirect.com/science/article/pii/S2352152X23004322.

[24] Wang H, Wang F, Wang B, Wu J, Lu H, Wang C. Partial flow separation in guide-vane region of large-capacity/low-head pumped hydro energy storage system with horizontal shaft. J Energy Storage 2023;71:108173. http://dx.doi.org/10.1016/j.est.2023.108173, https://www.sciencedirect.com/science/article/pii/S2352152X23015700.

[25] Hoffstaedt J, Ansorena Ruiz R, Schürenkamp D, Jarquin Laguna A, Goseberg N. Experimental setup and methods for a novel low-head pumped storage system. In: 7th offshore energy & storage symposium (OSES 2023). IET Digital Library; 2023, p. 341–8.

[26] Riedelbauch S, Stens C. Pump to turbine transient for a pump-turbine in a model test circuit and a real size power plant. IOP Conf Ser: Earth Environ Sci 2019;240(7):072039. http://dx.doi.org/10.1088/1755-1315/240/7/072039.

[27] Zhu B, Wang X, Tan L, Zhou D, Zhao Y, Cao S. Optimization design of a reversible pump–turbine runner with high efficiency and stability. Renew Energy 2015;81:366–76. http://dx.doi.org/10.1016/j.renene.2015.03.050, https://www.sciencedirect.com/science/article/pii/S0960148115002323.

[28] Dixon S, Hall C. Chapter 2 - dimensional analysis: Similitude. In: Dixon S, Hall C, editors. Fluid mechanics and thermodynamics of turbomachinery (seventh edition). seventh ed.. Boston: Butterworth-Heinemann; 2014, p. 39–67. http://dx.doi.org/10.1016/B978-0-12-415954-9.00002-4, https://www.sciencedirect.com/science/article/pii/B9780124159549000024.

[29] Fahlbeck J, akan Nilsson H, Salehi S. Surrogate based optimisation of a pump mode startup sequence for a contra-rotating pump-turbine using a genetic algorithm and computational fluid dynamics. J Energy Storage 2023;62:106902. http://dx.doi.org/10.1016/j.est.2023.106902, https://www.sciencedirect.com/science/article/pii/S2352152X23002992.

[30] Fahlbeck J, Nilsson Ha, Salehi S. Surrogate based optimisation of a pump mode startup sequence for a contra-rotating pump-turbine using a genetic algorithm and computational fluid dynamics. J Energy Storage 2023;62:106902. http://dx.doi.org/10.1016/j.est.2023.106902.

[31] Schiesser WE. The numerical method of lines: integration of partial differential equations. Elsevier; 2012.

[32] Wylie E, Streeter V. Fluid transients in systems. J Fluid Mech 1994;264:375.

[33] Stecki JS, Davis DC. Fluid transmission lines-distributed parameter models part 1: a review of the state of the art. Proc Inst Mech Engrs. Part A 1986;200(A4, 1986):215–28.

[34] Ghidaoui MS, Zhao M, McInnis DA, Axworthy DH. A review of water hammer theory and practice. Appl Mech Rev 2005;58(1):49–76.

[35] Chaudhry MH. Applied hydraulic transients. Springer; 2014, http://dx.doi.org/10.13182/nt81-a32632.

[36] Tao R, Wang Z. Comparative numerical studies for the flow energy dissipation features in a pump-turbine in pump mode and turbine mode. J Energy Storage 2021;41:102835. http://dx.doi.org/10.1016/j.est.2021.102835, https://www.sciencedirect.com/science/article/pii/S2352152X21005600.

[37] Rehman S, Al-Hadhrami LM, Alam MM. Pumped hydro energy storage system: A technological review. Renew Sustain Energy Rev 2015;44:586–98. http://dx.doi.org/10.1016/j.rser.2014.12.040.

[38] Hahn H, Hau D, Dick C, Puchta M. Techno-economic assessment of a subsea energy storage technology for power balancing services. Energy 2017;133:121–7. http://dx.doi.org/10.1016/j.energy.2017.05.116, https://www.sciencedirect.com/science/article/pii/S0360544217308733.

[39] Berrada A, Emrani A, Ameur A. Life-cycle assessment of gravity energy storage systems for large-scale application. J Energy Storage 2021;40:102825. http://dx.doi.org/10.1016/j.est.2021.102825, https://www.sciencedirect.com/science/article/pii/S2352152X2100551X.

[40] Menéndez J, Fernández-Oro JM, Galdo M, Loredo J. Efficiency analysis of underground pumped storage hydropower plants. J Energy Storage 2020;28:101234. http://dx.doi.org/10.1016/j.est.2020.101234, https://www.sciencedirect.com/science/article/pii/S2352152X20300323.

[41] Ida T. Analysis of scale effects on performance characteristics of hydraulic turbines. J Hydraul Res 1990;28(1):93–104. http://dx.doi.org/10.1080/00221689009499149, arXiv:DOI:10.1080/00221689009499149.

[42] Ida T, Kubota T, Kurokawa J, Tanaka H. Recent development of studies on scale effect. In: Cabrera E, Espert V, Martínez F, editors. Hydraulic machinery and cavitation. Dordrecht: Springer Netherlands; 1996, p. 313–22.

[43] White FM. Fluid mechanics, eighth ed. New York: McGraw-Hill Education; 2016.